Journal of Zhejiang University-SCIENCE A in press
www.jzus.zju.edu.cn; www.springer.com/journal/11582
E-mail: jzus_a@zju.edu.cn

Research Article
https://doi.org/10.1631/jzus.A2600073

Comparative assessment of finite element formulations for dynamic analysis in low-permeability saturated porous media

Anhao PAN[1,2], Daosheng LING[1,2]✉, Xiao MIAO[1,2], Jianjing ZHENG[2,3]

[1]*Institute of Geotechnical Engineering, Zhejiang University, Hangzhou 310058, China*
[2]*MOE Key Laboratory of Soft Soils and Geoenvironmental Engineering, Zhejiang University, Hangzhou 310058, China*
[3]*Center for Hypergravity Experimental and Interdisciplinary Research, Zhejiang University, Hangzhou 310058, China*

Abstract: To address the issue of spurious pore pressure oscillations in equal-order finite element analyses of dynamic responses of low-permeability saturated porous media, we compare two primary formulations: (1) a novel unequal-order interpolation element enriched with cover functions, and (2) a stabilized equal-order interpolation element. To circumvent inherent linear dependence issues in the cover function-enriched formulation, specialized quadrilateral and triangular elements are developed for 1D and 2D problems, respectively. The performance of each element type is evaluated for both compressible and incompressible materials. Our results demonstrate that the cover element consistently and accurately captures pore pressure evolution for both forms of material. In contrast, the stabilized equal-order element achieves acceptable accuracy only for incompressible materials with high skeleton stiffness, and exhibits degraded performance for compressible materials. Despite efforts to mitigate the influence of the stabilization term, the numerical results remain prone to either oscillatory or excessively damped responses.

Key words: Cover function; Linear dependence; Unequal-order element; Stabilized element; Pressure oscillations

1 Introduction

Since Biot (1956a, 1956b) established wave propagation theory for saturated porous media, high-precision calculation of pore pressure has remained fundamental for characterizing the dynamic response of saturated soils under dynamic loading, for instance during seismic excitation. When the motion inertia of pore fluid relative to the solid skeleton can be neglected, the *u-p* formulation of Biot's theory for saturated porous media is widely employed (Zienkiewicz et al., 1980). Nevertheless, a finite element method using equal-order interpolation for displacement and pore pressure cannot satisfy the so-called Ladyzhenskaya-Babuška-Brezzi (LBB) conditions (Babuška, 1971) or inf-sup conditions (Bathe, 2001); this can cause severe unphysical oscillations in the pore pressure field. Addressing this problem has become a prominent topic in the field of porous media dynamic analysis.

Unequal-order interpolation elements, which interpolate displacement and pore pressure in different manners, are widely utilized in the analysis of porous media. Among these, the Taylor-Hood element (Taylor and Hood, 1973) remains the most commonly adopted. By increasing the number of displacement nodes, this element ensures that the interpolation order for displacement is one level higher than that for pore pressure, making it advantageous for porous media analysis (Sonntag et al., 2023; Staubach and Machaček, 2023; Xing and Zhao, 2023). An alternative approach to unequal-order interpolation elements is to reduce the pressure interpolation order. For example, a pseudo-randomly weighted piecewise-constant pressure approximation – where the pressure is constant on nodal subdomains – has been shown to achieve numerical stability in incompressible and nearly incompressible material flows (Feulvarch et al., 2023).

Instead of adding displacement nodes to improve

✉ Daosheng LING, dsling@zju.edu.cn
Daosheng LING, https://orcid.org/0000-0002-0604-1175

Received Feb. 1, 2026; Revision accepted Mar. 27, 2026; Crosschecked

the interpolation order, more attractive approaches include the numerical manifold method (NMM) (Shi, 1991) or the generalized finite element method (GFEM) (Melenk and Babuška, 1996), both of which introduce nodal cover functions (referred to as local approximations in GFEM) to enrich the approximation space. Related to this, Yun et al. (2023) conducted a detailed comparison of the stability and accuracy of cover elements with different interpolation orders, showing that cover elements are insensitive to mesh distortion and offer higher accuracy. Moreover, assuming that the solid and fluid phases were compressible, Zhang and Zhou (2006) adopted the NMM in the *u-p* formulation – with the displacement field one order higher than the pore pressure – to simulate the dynamic response of saturated porous media under nearly undrained conditions, and validated the effectiveness of the NMM for pressure oscillation problems. Based on the *u-w-p* formulation, Wu et al. (2019a, 2019b) employed the NMM with solid displacement and the fluid velocity interpolations one order higher than the pore pressure interpolation, investigating wave propagation in cracked media with incompressible solid and fluid phases. Another advantage of using nodal cover functions is that they can be specifically constructed based on the characteristics of known solutions to the problem, thereby improving the accuracy. Inspired by the trigonometric properties of analytical solutions for wave propagation problems, trigonometric-type nodal cover functions have been employed for displacement enrichment to suppress spurious oscillations (Ham and Bathe, 2012; Gui et al., 2023; Tang et al., 2024). Subsequently, nodal displacement cover functions combining high-order and trigonometric properties have been applied to accurately simulate the transient wave propagation process (Kim et al., 2018; Chai and Bathe, 2020; Chai et al., 2022; Gui et al., 2023, 2024; Xue et al., 2024).

Stabilization methods have been shown to effectively reduce pressure oscillations by incorporating an artificial stabilization term into the governing equations. Initially proposed by Hafez and Soliman (1993), the Direct-Alpha method modifies overall governing equations by introducing a stabilization term into the continuity equation. This term is formulated as the divergence of the momentum balance equation, multiplied by a constant determined based on the mesh size. Building upon this foundation, Pastor et al. (1997) modified the stabilization term to include the time derivative of the divergence of the momentum balance equation. The effectiveness of this method in suppressing pressure oscillations for dynamic analysis of incompressible saturated media under undrained conditions was accordingly validated. Subsequent studies extended the methodology to three dimensions and applied it in various engineering contexts (McGann et al., 2015; Corciulo et al., 2017; Kementzetzidis et al., 2019).

Another stabilization method, the Polynomial Pressure Projection technique (PPP), mitigates pressure instability arising from equal-order interpolation by mapping the local pore pressure field of the elements. Assuming that the solid and fluid phases are incompressible, White and Borja (2008) employed the PPP technique in the context of static consolidation of porous media to satisfy the LBB condition and effectively suppress spurious pore pressure oscillations in the fault region. Later, Guo et al. (2019) and Gavagnin et al. (2020) applied the PPP technique to simulate static crack growth in saturated porous media, effectively resolving the issue of global pore pressure oscillations (particularly at the crack itself) for incompressible materials. For two-phase compressible media, Sun et al. (2013) and Li et al. (2018) employed the PPP technique in static analyses and adjusted the form of the stabilization parameter to improve the accuracy. Regarding incompressible materials and dynamic analysis of three-dimensional elastic-plastic saturated porous media, Hao et al. (2023) utilized reduced integration and PPP to solve the problem of pore pressure oscillations of equal-order linear interpolation under the undrained limit. Spurious pressure oscillations also occur in contact problem simulations. For instance, Liu and Borja (2010) employed PPP to resolve pressure oscillations in frictional contact problems. Moreover, using the cohesive zone model to describe strong discontinuity, Liu (2020) adopted PPP to prevent spurious oscillations in the pressure field.

As an alternative approach, the fractional step algorithm is commonly employed for incompressible porous media to suppress spurious pore pressure oscillations. To some extent, the fractional step algorithm is a stabilization method; as Huang et al. (2004) noted, it is equivalent to introducing a

stabilization term into the steady-state approximation. With the introduction of an intermediate acceleration term for solids, semi-explicit algorithms (Zienkiewicz et al., 1993) and staggered implicit-implicit fractional step algorithms (Huang and Zienkiewicz, 1998; Huang et al., 2001; Huang et al., 2004) were proposed and applied to dynamic analysis using the *u-p* formulation. Notably, Zienkiewicz et al. (1993) pointed out that in the dynamic analysis of saturated porous media, the equilibrium equation should first be discretized in time, then intermediate variables should be introduced to split the equation, and finally spatial discretization should be performed. Furthermore, Markert et al. (2010) compared the monolithic implicit algorithm with a semi-explicit-implicit fractional step algorithm, and found that the former was superior in terms of computational accuracy and stability. In recent years, fractional step algorithms have been enhanced to suppress numerical oscillations in both incompressible (Kularathna et al., 2021; Yuan et al., 2023; Hidano et al., 2024) and compressible (Yuan et al., 2022; Yu et al., 2025) problems in dynamic analysis when using the material point method.

In summary, although various methods have demonstrated effective suppression of spurious pore pressure oscillations, their accuracy largely remains limited to specific validation conditions. A comprehensive assessment of their robustness for compressible and incompressible materials in saturated porous media has yet to be conducted. Crucially, spurious pressure oscillations persist in low-permeability simulations employing equal-order interpolation, irrespective of elastic wave propagation differences between compressible and incompressible media. Accordingly, in this study we employ three different element types – standard equal-order, stabilized equal-order, and cover function-enriched unequal-order – for the dynamic analysis of saturated porous media. A systematic comparison is presented to assess the fidelity and effectiveness of each method for both compressible and incompressible materials.

2 Methodology

2.1 Governing equations

Under the assumption that the fluid inertia relative to the solid is negligible, the strong form of the governing equations for a two-phase saturated porous medium in the *u-p* formulation consists of the momentum balance and the pore fluid continuity equations, expressed as:

$$\boldsymbol{L}^{\mathrm{T}}\left(\boldsymbol{\sigma}'-\alpha\mathbf{m}p\right)-\rho\ddot{\boldsymbol{u}}+\rho\boldsymbol{b}=\mathbf{0} \tag{1}$$

$$\alpha\mathbf{m}^{\mathrm{T}}\boldsymbol{L}\dot{\boldsymbol{u}}+\frac{1}{Q_{\mathrm{b}}}\dot{p}-\boldsymbol{\nabla}^{\mathrm{T}}\left[k\gamma_{\mathrm{f}}^{-1}(\boldsymbol{\nabla}p-\rho_{\mathrm{f}}\boldsymbol{b})\right]=\mathbf{0} \tag{2}$$

Here, $\boldsymbol{u}$ is the solid skeleton displacement vector; $\ddot{\boldsymbol{u}}$ and $\dot{\boldsymbol{u}}$ represent the acceleration and velocity of the solid skeleton, respectively; p is the pore pressure, and $\dot{p}$ denotes its time derivative; $Q_{\mathrm{b}}=\left[\left(\alpha-n\right)/K_{\mathrm{s}}+n/K_{\mathrm{f}}\right]^{-1}$ is Biot's modulus reflecting the compressibility of solid particles and pore fluid, where K_{s} and K_{f} are the bulk moduli of the solid and fluid phases, respectively; k denotes the permeability coefficient; n is the porosity; γ_{f} represents the unit weight of the fluid; $\boldsymbol{b}$ is the gravitational acceleration; $\alpha=1-K_{\mathrm{D}}/K_{\mathrm{s}}$ represents the Biot coefficient; K_{s} and K_{D} are the bulk moduli of the solid particles and the skeleton, respectively, with $K_{\mathrm{D}}=\lambda+\frac{2}{3}G$; λ and G are the Lamé parameters; $\rho=\left(1-n\right)\rho_{\mathrm{s}}+n\rho_{\mathrm{f}}$ denotes the average density of the saturated porous media, with ρ_{s} and ρ_{f} being the density of the solid and fluid phases, respectively; for a plane stress condition, the effective stress vector is $\boldsymbol{\sigma}'=\{\sigma_x',\sigma_y',\tau_{xy}'\}^{\mathrm{T}}$ and the constant vector is $\mathbf{m}=\left\{1,1,0\right\}^{\mathrm{T}}$; for a plane strain condition, the effective stress vector is $\boldsymbol{\sigma}'=\{\sigma_x',\sigma_y',\sigma_z',\tau_{xy}'\}^{\mathrm{T}}$ and the constant vector is $\mathbf{m}=\left\{1,1,1,0\right\}^{\mathrm{T}}$; finally, $\boldsymbol{L}=\left[\begin{Bmatrix}\frac{\partial}{\partial x} & 0 & \frac{\partial}{\partial y}\end{Bmatrix},\begin{Bmatrix}0 & \frac{\partial}{\partial y} & \frac{\partial}{\partial x}\end{Bmatrix}\right]^{\mathrm{T}}$ and $\boldsymbol{\nabla}=\begin{bmatrix}\frac{\partial}{\partial x} & \frac{\partial}{\partial y}\end{bmatrix}^{\mathrm{T}}$ are linear operators.

Applying the standard Galerkin method for spatial discretization, the governing equations can be expressed in matrix form:

$$\begin{bmatrix} \boldsymbol{K}_{\mathrm{s}} & -\boldsymbol{K}_{\mathrm{sf}} \\ \boldsymbol{0} & \boldsymbol{K}_{\mathrm{f}} \end{bmatrix} \boldsymbol{d} + \begin{bmatrix} \boldsymbol{0} & \boldsymbol{0} \\ \boldsymbol{K}_{\mathrm{sf}}{}^{\mathrm{T}} & \boldsymbol{H}_{\mathrm{f}} \end{bmatrix} \dot{\boldsymbol{d}} + \begin{bmatrix} \boldsymbol{M}_{\mathrm{s}} & \boldsymbol{0} \\ \boldsymbol{0} & \boldsymbol{0} \end{bmatrix} \ddot{\boldsymbol{d}} = \begin{Bmatrix} \boldsymbol{F}_{\mathrm{s}} \\ \boldsymbol{F}_{\mathrm{f}} \end{Bmatrix} \quad (3)$$

The specific forms of the submatrices in Eq. (3) and the boundary conditions can be found in Section S1.1 of the electronic supplementary materials (ESM).

Then, the Newmark method is utilized for temporal integration of the discretized system described by Eq. (3). Further details on the time discretization are provided in Section S1.2 of the ESM. To ensure integration accuracy and algorithmic stability, the parameters δ and β of the Newmark method should satisfy the following conditions:

$$\delta \geq 0.50\,,\ \beta \geq 0.25\left(0.5+\delta\right)^2 \quad (4)$$

Referring to previous studies (Kontoe et al., 2008; Monforte et al., 2019; Zhao and Choo, 2020), we set δ and β to 0.6 and 0.3025, respectively.

2.2 Stabilized equal-order interpolation element

Stabilization techniques mitigate spurious pore pressure oscillations in equal-order formulations by introducing artificial stabilization terms into the continuity equation, so as to satisfy the LBB condition. Among these, the Polynomial Pressure Projection (PPP) technique is a common and robust strategy.

The core concept of PPP involves computing the average of the element shape functions and the element pore pressure at the elemental level. First, a constant projection operator corresponding to the element pore pressure is defined as:

$$\Pi\left(p^{\mathrm{h}}\right) = \frac{1}{V^{\mathrm{e}}} \int_{\Omega^{\mathrm{e}}} p^{\mathrm{h}} \mathrm{d}\Omega \quad (5)$$

where Ω^{e} and V^{e} are the area and volume of the element, respectively. The projecting field value for each element is equal to the mean value of the field within that element, such that the projection operator obtains the mean pore pressure at the elemental level. Subsequently, the stabilization term added to the continuity equation is:

$$\boldsymbol{H}_{\mathrm{p}} = \int_{\Omega} \frac{\tau}{2G} [\boldsymbol{N}_p - \Pi(\boldsymbol{N}_p)]^{\mathrm{T}} [\boldsymbol{N}_p - \Pi(\boldsymbol{N}_p)] \mathrm{d}\Omega \quad (6)$$

where G is the shear modulus and τ is the stabilization parameter that regulates the magnitude of the stabilization term. The stabilization parameter τ is set to 1.0 in this paper unless otherwise specified. In addition to the form $\frac{\tau}{2G}$, various scholars (Sun et al., 2013; Li and Wei, 2018; Monforte et al., 2019; Gavagnin et al., 2020; Wang et al., 2023) have proposed alternative stabilization parameter forms to obtain higher accuracy.

After the stabilization term is added, the governing equations are:

$$\begin{bmatrix} \boldsymbol{K}_{\mathrm{s}} & -\boldsymbol{K}_{\mathrm{sf}} \\ \boldsymbol{0} & \boldsymbol{K}_{\mathrm{f}} \end{bmatrix} \boldsymbol{d} + \begin{bmatrix} \boldsymbol{0} & \boldsymbol{0} \\ \boldsymbol{K}_{\mathrm{sf}}{}^{\mathrm{T}} & \boldsymbol{H}_{\mathrm{f}} + \boldsymbol{H}_{\mathrm{p}} \end{bmatrix} \dot{\boldsymbol{d}} + \begin{bmatrix} \boldsymbol{M}_{\mathrm{s}} & \boldsymbol{0} \\ \boldsymbol{0} & \boldsymbol{0} \end{bmatrix} \ddot{\boldsymbol{d}} = \begin{Bmatrix} \boldsymbol{F}_{\mathrm{s}} \\ \boldsymbol{F}_{\mathrm{f}} \end{Bmatrix} \quad (7)$$

Besides the PPP technique, a variety of other stabilization techniques (Oñate, 2000; Truty and Zimmermann, 2006; Aguilar et al., 2008; de Pouplana and Oñate, 2017; He et al., 2025) have been proposed and utilized in various applications. Although the derivation procedure and the form of the stabilization term differ for these methods, the essence of the stabilization method is still to add an artificial stabilization term to modify the governing equations and to control this term's magnitude through the stabilization parameter. In this study, the PPP technique is employed as a representative in order to validate the accuracy of these types of methods.

2.3 Unequal-order interpolation element

2.3.1 Cover function-enriched element

Two strategies exist for unequal-order interpolation. The first employs the conventional finite element framework with distinct nodes for displacement and pore pressure (i.e., Taylor-Hood elements); this yields quadratic displacement and linear pore pressure interpolation, as illustrated in Fig. 1(a). The second utilizes identical interpolation nodes for both fields but employs nodal cover functions, with the displacement cover function being one order higher than that of pore pressure, as depicted in Fig. 1(b). Compared to the first strategy, the second is more versatile.

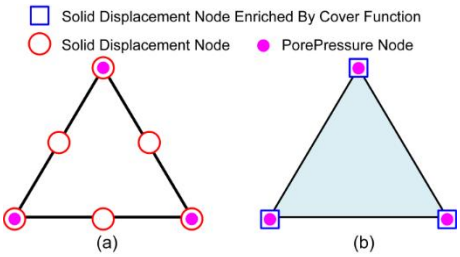

Fig. 1 The unequal-order elements: (a) Taylor-Hood Element; (b) cover function-enriched element

According to the NMM, displacement and pore pressure interpolation of the elements can be represented as:

$$N_{ui}=N_{pi}=N_i,\ \boldsymbol{u}^{\mathrm{e}}=\sum_{i=1}^{n}N_i\boldsymbol{C}_{ui}^{\mathrm{e}},\ p^{\mathrm{e}}=\sum_{i=1}^{n}N_iC_{pi}^{\mathrm{e}} \quad (8)$$

where $\boldsymbol{C}_{ui}^{\mathrm{e}}=\left\{C_{ui}^{\mathrm{e}},C_{vi}^{\mathrm{e}}\right\}^{\mathrm{T}}$ and C_{pi}^{e} are the skeleton displacement nodal cover function and pore pressure nodal cover function, respectively. The nodal cover function typically takes a polynomial form, and can be expressed as:

$$\boldsymbol{C}_{ui}^{\mathrm{e}}=\boldsymbol{P}_{ui}\boldsymbol{d}_{ui}^{\mathrm{e}},\ C_{pi}^{\mathrm{e}}=\boldsymbol{P}_{pi}\boldsymbol{d}_{pi}^{\mathrm{e}} \quad (9)$$

in which:

$$\boldsymbol{P}_{ui}=\begin{bmatrix}\bar{\boldsymbol{P}}_i^{n_u} & \boldsymbol{0}\\ \boldsymbol{0} & \bar{\boldsymbol{P}}_i^{n_u}\end{bmatrix},\ \boldsymbol{d}_{ui}^{\mathrm{e}}=\begin{Bmatrix}\boldsymbol{d}_{ui}^{\prime\mathrm{e}}\\ \boldsymbol{d}_{vi}^{\prime\mathrm{e}}\end{Bmatrix},\ \boldsymbol{P}_{pi}=\bar{\boldsymbol{P}}_i^{n_p},\ \boldsymbol{d}_{pi}^{\mathrm{e}}=\boldsymbol{d}_{pi}^{\prime\mathrm{e}} \quad (10)$$

Here, n_u and n_p are the orders of the nodal cover functions of skeleton displacement and pore pressure, respectively; $\bar{\boldsymbol{P}}_i^k$ is the k^{th} order polynomial vector of node i; $\boldsymbol{d}_{ui}^{\mathrm{e}}$ and $\boldsymbol{d}_{pi}^{\mathrm{e}}$ are the nodal degrees of freedom vectors of skeleton displacement and pore pressure, respectively. The cover function-enriched element degenerates to the standard equal-order element method when all cover functions are of order zero.

In this study, the first-order and zero-order cover functions are employed for skeleton displacement and pore pressure, respectively. There are six displacement degrees of freedom and one pore pressure degree of freedom on one node, i.e.:

$$\begin{cases}\bar{\boldsymbol{P}}_{ui}^{1}=\left\{1,x-x_i,y-y_i\right\},\ \boldsymbol{d}_{ui}^{\prime\mathrm{e}}=\left\{u_i^{00},u_i^{10},u_i^{01}\right\}^{\mathrm{T}},\ \boldsymbol{d}_{vi}^{\prime\mathrm{e}}=\left\{v_i^{00},v_i^{10},v_i^{01}\right\}^{\mathrm{T}}\\ \bar{\boldsymbol{P}}_{pi}^{0}=\left\{1\right\},\ \boldsymbol{d}_{pi}^{\prime\mathrm{e}}=\left\{p_i^{00}\right\}\end{cases} \quad (11)$$

By substituting Eq. (9) into Eq. (8), the element displacement and pore pressure interpolations based on nodal cover functions can be expressed as:

$$\boldsymbol{u}^{\mathrm{e}}=\sum_{i=1}^{n}N_i\boldsymbol{P}_{ui}\boldsymbol{d}_{ui}^{\mathrm{e}},\ p^{\mathrm{e}}=\sum_{i=1}^{n}N_i\boldsymbol{P}_{pi}\boldsymbol{d}_{pi}^{\mathrm{e}} \quad (12)$$

Substituting Eq. (12) into Eqs. (1) and (2) and applying the Galerkin spatial discretization method yields the submatrices of the discretized cover element, as detailed in Section S.1.3 of the ESM.

2.3.2 Linear dependence issues and the imposition of boundary conditions

When both the shape function and the nodal cover function of the element are complete polynomials, there exist well-known linear dependence issues in NMM/GFEM, resulting in the singularity of the stiffness matrix. Taking the first-order triangular cover element as an example, its cover polynomial vector is:

$$\bar{\boldsymbol{P}}_i^{1}=\left\{1,x-x_i,y-y_i\right\} \quad (13)$$

Consequently, a single triangular cover element possesses nine degrees of freedom (DOFs) in each direction. The polynomial resulting from the product of the element shape function and the cover function is comprised of the following six terms:

$$\left\{1\quad x\quad y\quad x^2\quad xy\quad y^2\right\} \quad (14)$$

Therefore, the total rank deficiency in both directions is given by $R_{\mathrm{d}}=2(9-6)=6$, indicating that the stiffness matrix contains six redundant DOFs.

As the number of triangular cover elements increases, the rank deficiency of the triangular mesh does not increase (Tian et al., 2006; An et al., 2011). As illustrated in Fig. 2, each time a new element is added, the number of newly introduced DOFs remains consistent between Taylor-Hood elements and cover elements. This demonstrates that the rank deficiency associated with triangular cover elements

remains constant regardless of the total number of elements.

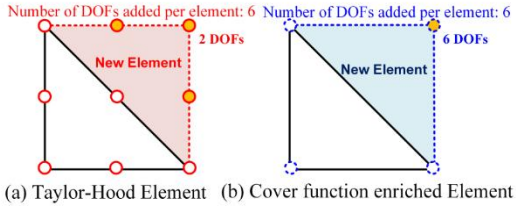

Fig. 2 Variation in DOFs: (a) Taylor-Hood element; (b) cover function-enriched element

In this study, first-order polynomials are employed as the displacement cover functions for the triangular cover elements. For 2D problems, the global triangular mesh is characterized by a rank deficiency of $R_{\mathrm{d}}=6$, which implies that linear independence of the global stiffness matrix can be achieved through the proper constraint of just six DOFs (degrees of freedom). The imposition of boundary conditions for triangular cover elements is depicted in Fig. 3. Nodes 1, 2, and 3 correspond to three distinct types of boundary treatments:

(1) Node Type 1: For nodes where only displacement in a single direction (either the x- or y-direction) is constrained, the corresponding three DOFs in that direction are restricted.

(2) Node Type 2: For nodes where displacements in both the x- and y-directions are constrained, all six DOFs are fully fixed.

(3) Node Type 3: For nodes that do not require any boundary conditions, all DOFs remain unconstrained.

In 2D problems, at least two translational and one rotational DOF must be constrained to eliminate rigid body motion. The combined constraints imposed by Node Types 1 and 2 effectively suppress rigid body displacement and ensure that at least six redundant DOFs in the system are restricted. Moreover, these constraint rules are consistently applied to all triangular cover element nodes with prescribed boundary conditions. Consequently, the actual number of constrained DOFs far exceeds the theoretical minimum, thereby rigorously ensuring the full-rank property of the global stiffness matrix.

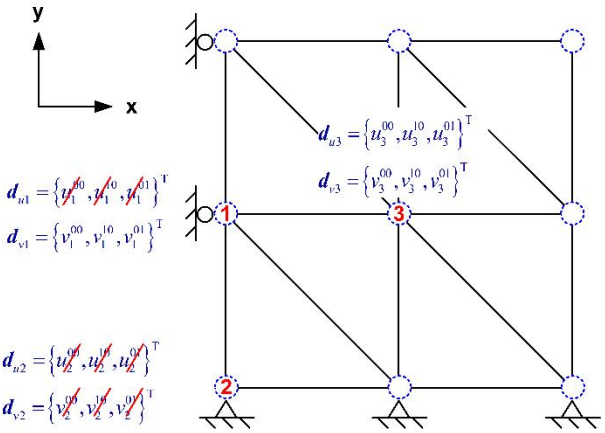

Fig. 3 Boundary conditions for the triangular cover elements

Conversely, when the cover polynomial vector of the quadrilateral element is a complete polynomial (i.e., $\bar{\boldsymbol{P}}_i^1=\{1,x-x_i,y-y_i,(x-x_i)(y-y_i)\}$), as shown in Fig. 4, the increment in the DOFs for the cover function-enriched elements exceeds that of the Taylor-Hood elements; therefore, the rank deficiency increases with the number of elements. In such cases, the DOF constraint method used for triangular cover elements is no longer applicable. Instead, it is usually necessary to reconstruct the nodal cover functions using approaches such as the least squares method (Rajendran and Zhang, 2007; Ma et al., 2022) to address the issue of linear dependence.

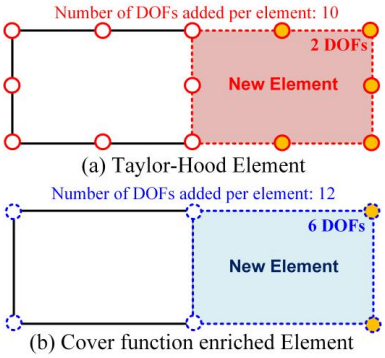

Fig. 4 Variation in DOFs caused by adding new quadrilateral elements: (a) Taylor-Hood element; (b) cover function-enriched element

This paper presents quadrilateral cover elements suitable for the 1D problem, in which the cover polynomial vector is defined as $\bar{\boldsymbol{P}}_{vi}^1=\{1,y-y_i\}$, and each node possesses two DOFs in the y-direction. As presented in Fig. 5, our analysis focuses on the 1D

case, where the rank deficiency of the global stiffness matrix is evaluated for meshes comprised of three different numbers of elements under various boundary conditions. The corresponding results are presented in Table 1. In Condition I, where no constraints are applied to Nodes 1 and 2, the rank deficiency of the global stiffness matrix for grids (a), (b), and (c) is the same; this indicates that the rank deficiency of the proposed 1D quadrilateral cover elements remains constant regardless of the number of elements. In condition II, where the DOFs v_1^{00} and v_2^{00} are constrained, the rank deficiency remains identical to that in Condition I. In Condition III, where all DOFs of Nodes 1 and 2 are fully constrained, the rank deficiency of the global stiffness matrix is eliminated. The above analysis demonstrates that constraining the DOFs v_1^{01} and v_2^{01} of Nodes 1 and 2 effectively eliminates the linear dependence in the stiffness matrix. This confirms the feasibility and applicability of the proposed quadrilateral cover elements for 1D problems.

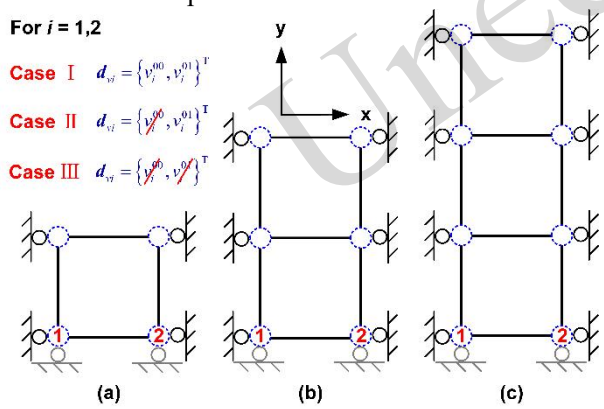

Fig. 5 Quadrilateral cover element meshes and boundary conditions in 1D problems

Table 1 Rank deficiency of the global stiffness matrix

1D quadrilateral cover element $\bar{\boldsymbol{P}}_{vi}^{1}=\{1, y-y_i\}$ $\boldsymbol{d}_{vi}^{\prime e}=\{v_i^{00}, v_i^{01}\}^{\mathrm{T}}$	Condition I	Condition II	Condition III
	No boundary conditions	DOF v_1^{00} and v_2^{00} of nodes 1 and 2 are constrained	Constrain all DOFs of nodes 1 and 2
Grid	Rank deficiency/Total number of DOFs		
(a)	2/8	2/6	0/4
(b)	2/12	2/10	0/8
(c)	2/16	2/14	0/12

The preceding analysis validates that the issue of linear dependence arising from high-order cover functions has been effectively addressed. Accordingly, in subsequent sections, quadrilateral cover elements are adopted in the 1D problems, while triangular cover elements are employed in the 2D problems.

Three element types are used in this study: the standard equal-order element (U1P1), the stabilized equal-order element (U1P1M), and the cover function-enriched element (U2P1). For the 1D benchmark cases, the conventional unequal-order Taylor-Hood element (TH-Quad) is also included as a comparative reference for U2P1. Details of the element geometry, type, and other parameters are summarized in Table S1 in the ESM.

3 Dynamic analysis of incompressible saturated porous media

3.1 Dynamic consolidation of a 1D incompressible elastic column

In incompressible saturated porous media, the Biot's modulus Q_{b} is infinite. A 1D plane strain elastic column is first considered for this case. The column has a height of 10 m and a width of 2 m. The upper surface is drained, whereas the bottom and lateral boundaries are impermeable; the bottom is fully fixed, with lateral normal displacements constrained. The material parameters utilized are listed in Table 2. A periodic load of $f(t)=3\left[1-\cos(75t)\right]$ kPa is subjected to the top surface. For comparison, the analytical solution proposed by De Boer et al. (1993) is used. The relative error of pore pressure is defined as:

$$\varepsilon_{\mathrm{p}}=\left|\frac{p-p_{\mathrm{ref}}}{p_{\mathrm{ref}}}\right| \tag{15}$$

where p and p_{ref} are the numerical solution value and the exact solution value, respectively. Moreover, the time step is $\Delta t=1\times10^{-4}$ s.

Table 2 Incompressible material parameters

Parameters	Values

Young's modulus E	20.1 MPa
Poison's ratio v	0.2
Porosity n	0.33
Unit weight of the fluid γ_f	10 kN/m^3
Solid density ρ_s	2000 kg/m^3
Fluid density ρ_f	1000 kg/m^3
Permeability coefficient k	1×10^{-12} m/s

The column is uniformly divided into 50 rectangular elements along the height direction. Fig. 6 illustrates the evolution of the pore pressure for the different elements at a height of 9 m with comparison to the analytical solution. The analytical solution is in close agreement with the load history, due to the permeability being so small that the pore pressure dissipation caused by consolidation at the top of the column is not discernible over such a short period. The pore pressure of U1P1 is approximately twice that of the analytical solution, and there are unphysical pore pressure oscillations throughout the entire column. In contrast, U1P1M, TH-Quad, and U2P1 exhibit good agreement with the analytical solution.

Next, the effect of the solid skeleton's compressibility on the performance of different elements is investigated. In the subsequent analyses, the column is discretized into 100 rectangular elements along the vertical direction. Fig. 7 presents the variation of relative pore pressure error with Young's modulus at a height of 9 m when t = 0.0419 s. Under varying skeleton compressibility, U2P1 consistently maintains high accuracy; TH-Quad exhibits larger errors when the skeletal stiffness is relatively high; and U1P1M shows larger errors under low skeletal stiffness. Furthermore, the sensitivity analyses presented in Section S2.2 of the ESM confirm that U2P1 maintains robust performance across varying element numbers and permeability coefficients.

We hypothesize that the relatively large errors observed in U1P1M under low skeleton stiffness conditions may be attributed to the stabilization term is too large. To further investigate this phenomenon, the stabilization parameter was systematically adjusted at E = 0.201 MPa. Fig. 8 shows the variation of the relative pore pressure error with the stabilization parameter; the results indicate that there is no clear monotonic relationship between the relative pore pressure error and the stabilization parameter. Consequently, choosing an appropriate stabilization parameter for different problems is a complex task. Furthermore, the accuracy for U1P1M does not attain the same level as U2P1, regardless of the adjustments made to the stabilization parameter.

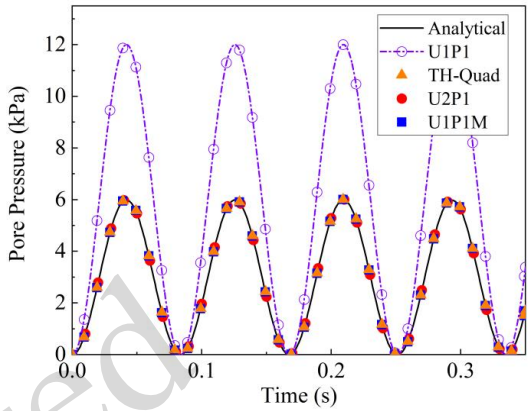

Fig. 6 Evolution of pore pressure at a height of 9 m

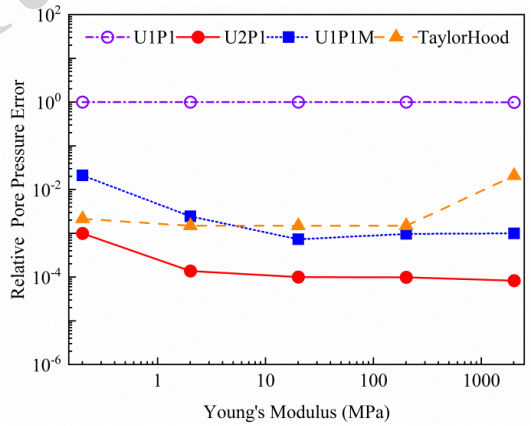

Fig. 7 Relative pore pressure error versus Young's modulus

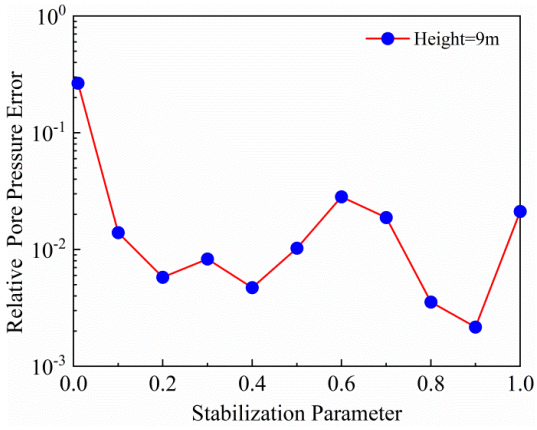

Fig. 8 Relative pore pressure error versus stabilization parameter of the U1P1M

3.2 Dynamic consolidation of 2D incompressible media

As illustrated in Fig. 9, the 2D plane strain model has dimensions of 21 m in width and 10 m in height. The model comprises a grid of 1,924 triangular elements, with a grid edge length of approximately 0.5 m. Four observation nodes, designated A, B, C, and D, are positioned at different heights in the middle of the model. The upper surface is drained, the two lateral surfaces and the bottom surface are impermeable, the bottom surface displacement is fully constrained, and the normal displacements of the two lateral surfaces are constrained. The material parameters follow those in Table 2, except that Young's modulus is set to 0.3 MPa or 30 MPa, with a porosity of $n=0.3$. A load of $f(t)=100\sin(25\pi t)\left[1-H\left(t-0.04\right)\right]$ kPa is applied uniformly over a width of 1 m at the center of the upper surface, where $H\left(t-0.04\right)$ is the Heaviside step function. The time step is $\Delta t=1\times10^{-5}$ s.

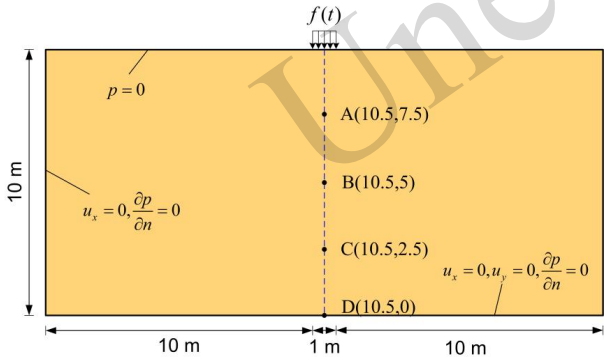

Fig. 9 Illustration of the 2D model

Figs. 10-11 present the contour plots of pore pressure at varying times when the Young's moduli E are 0.3 MPa and 30 MPa, respectively. As illustrated in Figs. 10(a) and 11(a), while the overall pore pressure response pattern for U1P1 closely resembles that for U2P1, U1P1 consistently exhibits pronounced pressure oscillations. As shown in Fig. 10 (E = 0.3 MPa), while the pore pressure field is quite stable in U1P1M, the pore pressure in U1P1M is notably smaller at t = 0.01 s and t = 0.02 s, and considerably larger at t = 0.03 s, compared to the other two elements. As demonstrated in Fig. 11, the pore pressures in U1P1M and U2P1 exhibit nearly equivalent trends when E = 30 MPa. Additional pore pressure histories at Nodes A and B are provided in Section S2.2 of the ESM, which support the above conclusions.

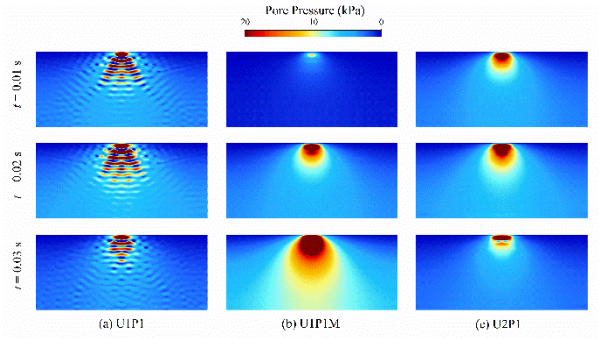

Fig. 10 Contours of pore pressure when E = 0.3 MPa

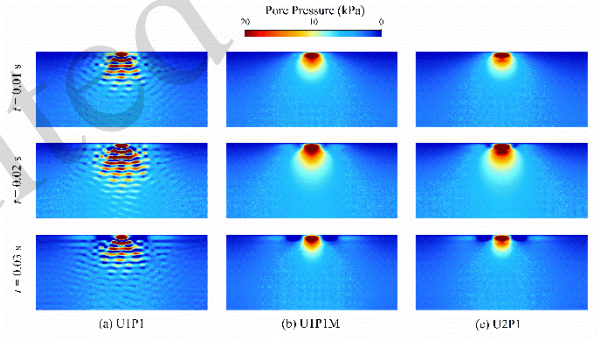

Fig. 11 Contours of pore pressure when E = 30 MPa

Considering the inferior performance exhibited by the U1P1M at E = 0.3 MPa – which can be attributed to the excess of the stabilization term – Fig. 12 illustrates the pore pressure field at various times with different stabilization parameters for the U1P1M. When $\tau=0.5$, the pore pressure field continues to change at a relatively slow rate, but with larger magnitude. When $\tau=0.1$, the overall trend of the pore pressure is similar to U2P1, but oscillations occur. This demonstrates the difficulty in determining a suitable stabilization parameter that is between the overly-stable and oscillatory states, suggesting that achieving U2P1 accuracy is almost impossible. This challenge is even more pronounced under extreme conditions like seismic liquefaction, where the soil stiffness can degrade to nearly zero. In such a severely softened state, the stabilization techniques which are typically designed for soils with non-negligible stiffness may prove ineffective, and consequently undermine the fidelity of pore pressure simulations.

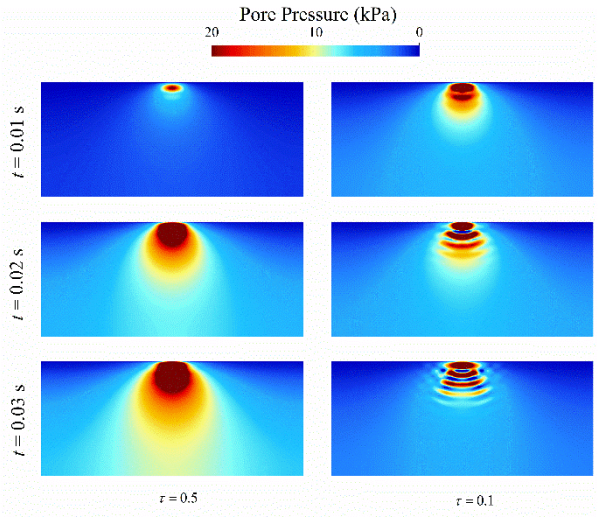

Fig. 12 Contours of pore pressure with different stabilization parameters when E = 0.3 MPa for U1P1M: (a) $\tau = 0.5$; (b) $\tau = 0.1$

4 Dynamic analysis of compressible saturated porous media

Under extremely low permeability, the propagation velocity of P1 waves within a compressible saturated porous media can be expressed as:

$$V_p = \sqrt{\frac{\lambda + 2G + \alpha^2 Q_b}{\rho}} \tag{16}$$

This enables the observation of transient processes induced by compressional wave propagation, such as pore pressure surge and wave reflection.

4.1 Dynamic consolidation of a compressible elastic column

The height of the 1D compressible plane strain elastic column is 30 m, and its width is 3 m. The same boundary conditions as in Section 3.1 are adopted. The material parameters employed are listed in Table 3. A step load of 1 kPa is applied to the top of the column, and the time step is $\Delta t = 1\times10^{-4}$ s. The analytical solutions derived by Shan et al. (2011) for 1D compression will be used as a reference.

Table 3. Compressible Material Parameters

Parameter	Value
Young's modulus, E	30 MPa
Poison's ratio, v	0.2
Porosity, n	0.3
Unit weight of the fluid, γ_f	10 kN/m^3
Solid density, ρ_s	2000 kg/m^3
Fluid density, ρ_f	1000 kg/m^3
Bulk modulus of the fluid, K_s	2 GPa
Bulk modulus of the solid, K_f	50 GPa
Permeability coefficient, k	1×10^{-12} m/s

Fig. 13 presents the evolution of pore pressure at a height of 27 m. The column is uniformly divided into 50 rectangular elements. The pore pressure for U1P1 is markedly higher than the analytical value. This suggests that equal-order elements continue to induce pressure oscillations in compressible saturated porous media. Although the results are more stable and the amount of pore pressure fluctuations becomes smaller with time, U1P1M is unable to accurately characterize the arrival and reflection of the compressional waves. U2P1 demonstrates satisfactory agreement with the analytical solution and accurately reflects the arrival and reflection of the P1 wave, despite minor pore pressure fluctuations which can be attributed to the limited number of elements. The results obtained from TH-Quad align closely with those of U2P1, but the former exhibits lower stability.

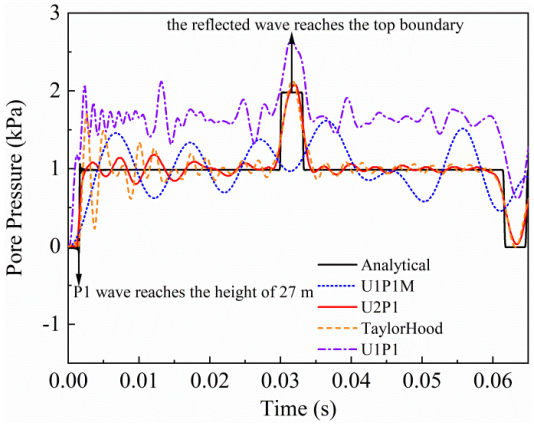

Fig. 13 Evolution of pore pressure at a height of 27 m

To investigate the influence of the size of the stabilization term on U1P1M, Fig. 14 presents the pore pressure profiles at t = 0.0317 s (when the reflected wave reaches the top surface) for varying stabilization parameters. The pore pressure shows pronounced oscillations between adjacent nodes of U1P1, especially near the top and bottom surfaces. TH-Quad suppresses pore pressure oscillations, although minor instabilities persist across the entire

height of the column. In contrast, U2P1 demonstrates the best performance, with only slight pore pressure oscillations occurring near the top of the column. When τ equals 1.0, despite there being no pronounced pore pressure oscillations between the adjacent nodes in U1P1M, the overall pore pressure distribution exhibits global oscillatory behavior along the height direction; this results in a significant discrepancy with the analytical solution. As the stabilization parameter gradually decreases, the amplitude of the global oscillations falls with it. However, the local pore pressure oscillations between the adjacent nodes gradually develop from the top drainage surface, eventually reaching a level similar to that of U1P1. Given these material properties, regardless of how the stabilization parameters are adjusted, a satisfactory result cannot be obtained, and the pore pressure field always remains in a state between global oscillation and local oscillation for U1P1M.

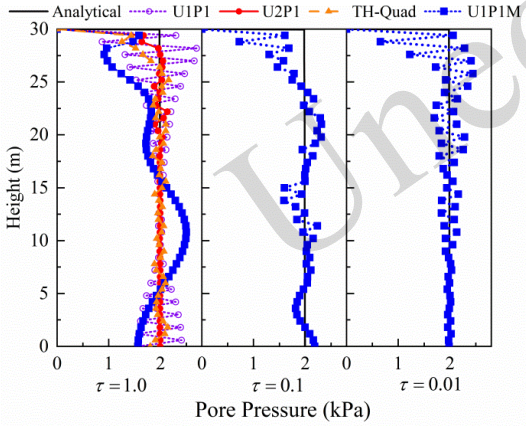

Fig. 14 Pore pressure profiles with different stabilization parameters at t = 0.0317 s

Fig. 15 depicts the relative error curves of pore pressure versus Young's modulus at a height of 27 m when the reflected wave reaches the top surface. A mesh of 100 elements is employed in the vertical direction. The relative error in pore pressure decreases with greater Young's modulus across all element types. U2P1 consistently maintains high accuracy, while TH-Quad and U1P1 exhibit comparable precision; U1P1M, however, always yields the lowest accuracy.

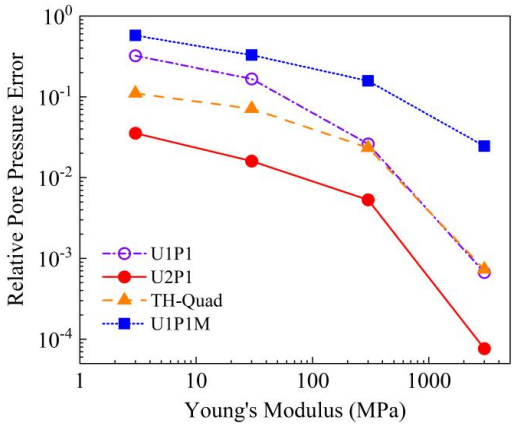

Fig. 15 Relative pore pressure error versus Young's modulus

4.2 Dynamic consolidation of 2D compressible media

The model configuration, mesh, and boundary conditions used here are identical to those described in Section 3.2. A uniform step load of 100 kPa is applied over a 1 m width at the center of the upper surface. The material parameters involved are given in Table 3. The time step is set to $\Delta t = 1\times10^{-5}$ s, and the stabilization parameter used for U1P1M is 0.1.

Fig. 16 presents the pore pressure contour plots at various times for the three elements. As illustrated in Fig. 16(a), although U1P1 captures the position of the wave front, the corresponding pore pressure field displays pronounced spurious oscillations, manifesting in the classical "checkerboard" pattern. The result from U1P1M is shown in Fig. 16(b). While this scheme remains highly stable and free from checkerboard oscillations, it severely overestimates the pore pressure dissipation, resulting in a diffuse wavefront and an underestimated wave velocity compared to the other two elements. In contrast, the result for U2P1 (displayed in Fig. 16(c)) clearly depicts the wave initiating from the loading area and propagating with a gradually expanding semicircular wavefront. The attenuation of pore pressure aligns with the dissipative nature of compressional waves, and the pore pressure increases as the wave reflects from the lower boundary. Under this condition of extremely low permeability, the theoretical velocity of the P1 wave calculated from Eq. (16) is 1898.5 m/s. The wave speed derived from the U2P1 simulation is approximately 1879.7 m/s, yielding an acceptable relative error of 0.992%. The pore pressure histories

of Nodes A, B, C, and D are provided in Section S3 of the ESM, further corroborating the superior accuracy of U2P1 in capturing wave propagation characteristics.

It is evident that when the stabilization parameter τ equals 0.1, the stabilization term is too large, ultimately rendering U1P1M overly stabilized. Fig. 17 depicts contour plots of pore pressure at t = 0.005 s, demonstrating the influence of varying the stabilization parameter for U1P1M. As the stabilization parameter decreases, the anomalous high attenuation of the compressional wave weakens, the wavefront becomes progressively clearer, and the wave velocity increases. However, pore pressure oscillations gradually intensify at the same time. These observations indicate that adjusting the stabilization parameter in U1P1M has a limited effect on improving the accuracy of the pore pressure field for compressible materials with low overall stiffness. This therefore highlights its inherent disadvantage in scenarios involving soft soils, or seismic conditions where the soil stiffness is significantly reduced.

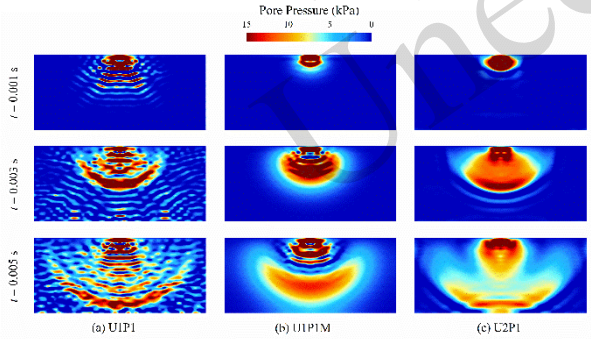

Fig. 16 Contours of pore pressure when E = 30 MPa

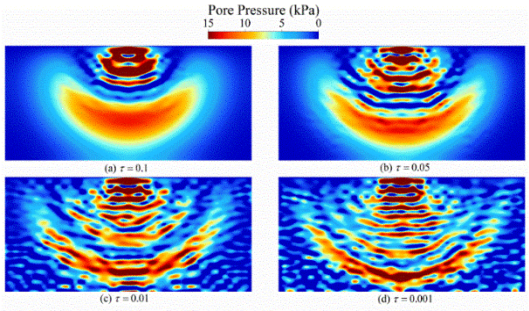

Fig. 17 Contours of pore pressure at t = 0.005 s versus the stabilization parameter when E = 30 MPa for the stabilized element U1P1M: (a) $\tau = 0.1$; (b) $\tau = 0.05$; (c) $\tau = 0.01$; (d) $\tau = 0.001$

5 Conclusions

In this study we investigated the challenge of spurious pore pressure oscillations during dynamic analysis of saturated porous media by evaluating two primary mitigation strategies. A comparative assessment was conducted among three types of finite elements: the standard equal-order element, the stabilized equal-order element, and the cover function-enriched unequal-order elements.

While the standard equal-order element can capture the general trend of pore pressure evolution in nearly undrained saturated porous media, it fails to suppress unphysical oscillations. This is true under both incompressible and compressible conditions.

The stabilized equal-order element is sensitive to the artificial stabilization terms, leading to an overestimation of compressional wave dissipation and an underestimation of wave velocity. Achieving a balance between accuracy and numerical stability remains challenging, even when the stabilization parameter is calibrated based on Young's modulus, mesh size, and other relevant factors. Notably, the adverse effects of the stabilization term are more pronounced in compressible media than in incompressible media. As a result, an acceptable accuracy level is only achieved for incompressible porous media with sufficiently rigid solid skeletons.

The cover function-enriched unequal-order element consistently and accurately captures the evolution of pore pressure for both compressible and incompressible media. When employed for dynamic analysis, this type of element maintains computational robustness, demonstrating insensitivity to variations in solid skeleton rigidity, compressibility of the solid and fluid phases, and permeability.

In summary, the cover function-enriched unequal-order element yields relatively satisfactory results across nearly all conditions, and can be easily degenerated to a standard finite element. Therefore, its use is strongly recommended for dynamic analysis of saturated porous media.

Acknowledgments

This paper is based on work supported by the National Natural Science Foundation of China (No. 51988101).

Author contributions

Anhao Pan and Daosheng LING contributed to the

conceptualization, formal analysis, and investigation. Anhao Pan, Xiao Miao and Jianjing Zheng contributed to the methodology. Daosheng LING provided the supervision and funding acquisition. Anhao Pan wrote the first draft of the manuscript. All authors read and approved the final version.

Conflict of interest

The authors declare that they have no conflict of interest.

References

Aguilar G, Gaspar F, Lisbona F, et al., 2008. Numerical stabilization of Biot's consolidation model by a perturbation on the flow equation. *International Journal for Numerical Methods in Engineering*, 75(11):1282-1300. https://doi.org/10.1002/nme.2295

An XM, Li LX, Ma GW, et al., 2011. Prediction of rank deficiency in partition of unity-based methods with plane triangular or quadrilateral meshes. *Computer Methods in Applied Mechanics and Engineering*, 200(5-8):665-674. https://doi.org/10.1016/j.cma.2010.09.013

Babuška I, 1971. Error-bounds for finite element method. *Numerische Mathematik*, 16(4):322-333. https://doi.org/10.1007/bf02165003

Bathe K, 2001. The inf–sup condition and its evaluation for mixed finite element methods. *Computers & Structures*, 79(2):243-252. https://doi.org/10.1016/S0045-7949(00)00123-1

Biot MA, 1956. Theory of Propagation of Elastic Waves in a Fluid-Saturated Porous Solid. I. Low-Frequency Range. *The Journal of the Acoustical Society of America*, 28(2):168-178. https://doi.org/10.1121/1.1908239

Biot MA, 1956. Theory of Propagation of Elastic Waves in a Fluid-Saturated Porous Solid. II. Higher Frequency Range. *The Journal of the Acoustical Society of America*, 28(2):179-191. https://doi.org/10.1121/1.1908241

Chai Y, Bathe K, 2020. Transient wave propagation in inhomogeneous media with enriched overlapping triangular elements. *Computers & Structures*, 237:106273. https://doi.org/10.1016/j.compstruc.2020.106273

Chai Y, Li W, Liu Z, 2022. Analysis of transient wave propagation dynamics using the enriched finite element method with interpolation cover functions. *Applied Mathematics and Computation*, 412:126564. https://doi.org/10.1016/j.amc.2021.126564

Corciulo S, Zanoli O, Pisanò F, 2017. Transient response of offshore wind turbines on monopiles in sand: role of cyclic hydro–mechanical soil behaviour. *Computers and Geotechnics*, 83:221-238. https://doi.org/10.1016/j.compgeo.2016.11.010

DE BOER, R., EHLERS, W., LIU, Z. One-Dimensional Transient Wave Propagation in Fluid-Saturated Incompressible Porous Media. 1993;63(1): 59-72. https://doi.org/10.1007/BF00787910

de Pouplana I, Oñate E, 2017. A FIC-based stabilized mixed finite element method with equal order interpolation for solid–pore fluid interaction problems. *International Journal for Numerical and Analytical Methods in Geomechanics*, 41(1):110-134. https://doi.org/10.1002/nag.2550

Feulvarch E, Brosse A, Vincent Y, 2023. An LBB-stable P1/RNP0 finite element based on a pseudo-random integration method for incompressible and nearly incompressible material flows. International Journal for Numerical Methods in Engineering, 124(24):5558-5573. https://doi.org/10.1002/nme.7361

Gavagnin C, Sanavia L, De Lorenzis L, 2020. Stabilized mixed formulation for phase-field computation of deviatoric fracture in elastic and poroelastic materials. *Computational Mechanics*, 65(6):1447-1465. https://doi.org/10.1007/s00466-020-01829-x

Gui Q, Li W, Chai Y, 2023. The enriched quadrilateral overlapping finite elements for time-harmonic acoustics. *Applied Mathematics and Computation*, 451:128018. https://doi.org/10.1016/j.amc.2023.128018

Gui Q, Li W, Chai Y, 2024. Improved modal analyses using the novel quadrilateral overlapping elements. *Computers & Mathematics with Applications*, 154:138-152. https://doi.org/10.1016/j.camwa.2023.11.027

Gui Q, Wang Y, You X, et al., 2023. Performance of the quadrilateral overlapping elements combined with implicit time integration method in solving the transient wave propagations. *Engineering Analysis with Boundary Elements*, 155:1013-1027. https://doi.org/10.1016/j.enganabound.2023.07.015

Guo G, Fall M, 2019. Modelling of preferential gas flow in heterogeneous and saturated bentonite based on phase field method. *Computers and Geotechnics*, 116:103206. https://doi.org/10.1016/j.compgeo.2019.103206

Hafez M, Soliman M, 1993. Numerical solution of the incompressible Navier–Stokes equations in primitive variables on unstaggered grids. In: MD Gunzberger, RA Nicolaides (eds), Incompressible Computational Fluid Dynamics. Cambridge University Press, Cambridge, p.183–201. https://doi.org/10.1017/CBO9780511574856.008

Ham S, Bathe K, 2012. A finite element method enriched for wave propagation problems. *Computers & Structures*, 94-95:1-12. https://doi.org/10.1016/j.compstruc.2012.01.001

Hao Q, Yu J, Wang X, et al., 2023. Stabilized low-order finite-element formulation for static and dynamic simulation of saturated soils based on a hybrid integration scheme. *Computers and Geotechnics*, 161:105596. https://doi.org/10.1016/j.compgeo.2023.105596

He L, Jing L, Feng M, 2025. New stabilized mixed finite element methods for two-field poroelasticity with low

permeability. *Applied Mathematics and Computation*, 494:129285. https://doi.org/10.1016/j.amc.2025.129285

Hidano S, Yamaguchi Y, Takase S, et al., 2024. Semi-implicit material point method for simulating infiltration-induced failure of unsaturated soil structures. *International Journal for Numerical and Analytical Methods in Geomechanics*, 48(10):2661-2699. https://doi.org/10.1002/nag.3750

Huang M, Wu S, Zienkiewicz OC, 2001. Incompressible or nearly incompressible soil dynamic behaviour: a new staggered algorithm to circumvent restrictions of mixed formulation. *Soil Dynamics & Earthquake Engineering*, 21(2):169-179. https://doi.org/10.1016/S0267-7261(00)00105-6

Huang M, Yue ZQ, Tham LG, et al., 2004. On the stable finite element procedures for dynamic problems of saturated porous media. *International Journal for Numerical Methods in Engineering*, 61(9):1421-1450. https://doi.org/10.1002/nme.1115

Huang M, Zienkiewicz OC, 1998. New unconditionally stable staggered solution procedures for coupled soil-pore fluid dynamic problems. *International Journal for Numerical Methods in Engineering*, 43(6):1029-1052. https://doi.org/10.1002/(SICI)1097-0207(19981130)43:6<1029::AID-NME459>3.0.CO;2-H

Kementzetzidis E, Corciulo S, Versteijlen WG, et al., 2019. Geotechnical aspects of offshore wind turbine dynamics from 3D non-linear soil-structure simulations. *Soil Dynamics and Earthquake Engineering*, 120:181-199. https://doi.org/10.1016/j.soildyn.2019.01.037

Kim K, Zhang L, Bathe K, 2018. Transient implicit wave propagation dynamics with overlapping finite elements. *Computers & Structures*, 199:18-33. https://doi.org/10.1016/j.compstruc.2018.01.007

Kontoe S, Zdravkovic L, Potts DM, 2008. An assessment of time integration schemes for dynamic geotechnical problems. *Computers and Geotechnics*, 35(2):253-264. https://doi.org/10.1016/j.compgeo.2007.05.001

Kularathna S, Liang W, Zhao T, et al., 2021. A semi-implicit material point method based on fractional-step method for saturated soil. *International Journal for Numerical and Analytical Methods in Geomechanics*, 45(10):1405-1436. https://doi.org/10.1002/nag.3207

Li W, Wei C, 2018. Stabilized low-order finite elements for strongly coupled poromechanical problems. *International Journal for Numerical Methods in Engineering*, 115(5):531-548. https://doi.org/10.1002/nme.5815

Liu F, 2020. Modeling hydraulic fracture propagation in permeable media with an embedded strong discontinuity approach. *International Journal for Numerical and Analytical Methods in Geomechanics*, 44(12):1634-1655. https://doi.org/10.1002/nag.3080

Liu F, Borja RI, 2010. Stabilized low-order finite elements for frictional contact with the extended finite element method. *Computer Methods in Applied Mechanics and Engineering*, 199(37):2456-2471. https://doi.org/10.1016/j.cma.2010.03.030

Ma J, Duan Q, Tian R, 2022. A generalized finite element method without extra degrees of freedom for large deformation analysis of three-dimensional elastic and elastoplastic solids. *Computer Methods in Applied Mechanics and Engineering*, 392:114639.

Markert B, Heider Y, Ehlers W, 2010. Comparison of monolithic and splitting solution schemes for dynamic porous media problems. *International Journal for Numerical Methods in Engineering*, 82(11):1341-1383. https://doi.org/10.1002/nme.2789

Mcgann CR, Arduino P, Mackenzie-Helnwein P, 2015. A stabilized single-point finite element formulation for three-dimensional dynamic analysis of saturated soils. *Computers and Geotechnics*, 66:126-141. https://doi.org/10.1016/j.compgeo.2015.01.002

Melenk JM, Babuška I, 1996. The partition of unity finite element method: Basic theory and applications. *Computer Methods in Applied Mechanics and Engineering*, 139(1):289-314. https://doi.org/10.1016/S0045-7825(96)01087-0

Monforte L, Navas P, Carbonell JM, et al., 2019. Low-order stabilized finite element for the full Biot formulation in soil mechanics at finite strain. *International Journal for Numerical and Analytical Methods in Geomechanics*, 43(7):1488-1515. https://doi.org/10.1002/nag.2923

Oñate E, 2000. A stabilized finite element method for incompressible viscous flows using a finite increment calculus formulation. *Computer Methods in Applied Mechanics and Engineering*, 182(3):355-370. https://doi.org/10.1016/S0045-7825(99)00198-X

Pastor M, Li T, Merodo JAF, 1997. Stabilized finite elements for harmonic soil dynamics problems near the undrained-incompressible limit. *Soil Dynamics and Earthquake Engineering*, 16(3):161-171. https://doi.org/10.1016/S0267-7261(97)00046-8

Rajendran S, Zhang BR, 2007. A "FE-meshfree" QUAD4 element based on partition of unity. *Computer Methods in Applied Mechanics and Engineering*, 197(1-4):128-147. https://doi.org/10.1016/j.cma.2007.07.010

Shan Z, Ling D, Ding H, 2011. Exact solutions for one-dimensional transient response of fluid-saturated porous media. *International Journal for Numerical and Analytical Methods in Geomechanics*, 35(4):461-479. https://doi.org/10.1002/nag.904

Shi, G. H., 1991. Manifold method of material analysis. Transactions of the 9th Army Conference on Applied Mathematics and Computing, Minneapolis. U.S. Army Research Office, p.57-76

Sonntag A, Wagner A, Ehlers W, 2023. Dynamic hydraulic

fracturing in partially saturated porous media. *Computer Methods in Applied Mechanics and Engineering*, 414:116121. https://doi.org/10.1016/j.cma.2023.116121

Staubach P, Machaček J, 2023. Separating fluid and solid contact constraints for hydro-mechanically coupled finite elements discretising fluid displacement. *Computer Methods in Applied Mechanics and Engineering*, 416:116451. https://doi.org/10.1016/j.cma.2023.116451

Sun W, Ostien JT, Salinger AG, 2013. A stabilized assumed deformation gradient finite element formulation for strongly coupled poromechanical simulations at finite strain. *International Journal for Numerical and Analytical Methods in Geomechanics*, 37(16):2755-2788. https://doi.org/10.1002/nag.2161

Tang T, Zhou W, Luo K, et al., 2024. Dynamic modeling and analysis of discontinuous wave propagation in a rod. *Journal of Sound and Vibration*, 569:117991. https://doi.org/10.1016/j.jsv.2023.117991

Taylor C, Hood P, 1973. A numerical solution of the Navier-Stokes equations using the finite element technique. *Computers and Fluids*, 1(1):73-100. https://doi.org/10.1016/0045-7930(73)90027-3

Tian R, Yagawa G, Terasaka H, 2006. Linear dependence problems of partition of unity-based generalized FEMs. *Computer Methods in Applied Mechanics and Engineering*, 195(37-40):4768-4782. https://doi.org/10.1016/j.cma.2005.06.030

Truty A, Zimmermann T, 2006. Stabilized mixed finite element formulations for materially nonlinear partially saturated two-phase media. *Computer Methods in Applied Mechanics and Engineering*, 195(13-16):1517-1546. https://doi.org/10.1016/j.cma.2005.05.044

Wang Z, Jin Y, Yin Z, et al., 2023. A dynamic SNS-PFEM with generalized-α method for hydro-mechanical coupled geotechnical problems. *Computers and Geotechnics*, 159:105466. https://doi.org/10.1016/j.compgeo.2023.105466

White JA, Borja RI, 2008. Stabilized low-order finite elements for coupled solid-deformation/fluid-diffusion and their application to fault zone transients. *Computer Methods in Applied Mechanics and Engineering*, 197(49-50):4353-4366. https://doi.org/10.1016/j.cma.2008.05.015

Wu W, Zheng H, Yang Y, 2019. Enriched three-field numerical manifold formulation for dynamics of fractured saturated porous media. *Computer Methods in Applied Mechanics and Engineering*, 353:217-252. https://doi.org/10.1016/j.cma.2019.05.008

Wu W, Zheng H, Yang Y, 2019. Numerical manifold method for dynamic consolidation of saturated porous media with three-field formulation. *International Journal for Numerical Methods in Engineering*, 120(6):768-802. https://doi.org/10.1002/nme.6157

Xing J, Zhao C, 2023. A hydro-mechanical phase field model for hydraulically induced fractures in poroelastic media. *Computers and Geotechnics*, 159:105418. https://doi.org/10.1016/j.compgeo.2023.105418

Xue H, Zhang X, Cheng J, 2024. Transient analyses of underwater acoustic propagation with the modified meshfree radial point interpolation method and newmark time integration techniques. *Ocean Engineering*, 304:117842. https://doi.org/10.1016/j.oceaneng.2024.117842

Yu J, Liang W, Zhao J, 2025. Enhancing dynamic modeling of porous media with compressible fluid: a THM material point method with improved fractional step formulation. *Computer Methods in Applied Mechanics and Engineering*, 444:118100. https://doi.org/10.1016/j.cma.2025.118100

Yuan W, Zheng H, Zheng X, et al., 2023. An improved semi-implicit material point method for simulating large deformation problems in saturated geomaterials. *Computers and Geotechnics*, 161:105614. https://doi.org/10.1016/j.compgeo.2023.105614

Yuan W, Zhu J, Liu K, et al., 2022. Dynamic analysis of large deformation problems in saturated porous media by smoothed particle finite element method. *Computer Methods in Applied Mechanics and Engineering*, 392:114724. https://doi.org/10.1016/j.cma.2022.114724

Yun G, Lee J, Kim D, 2023. Stability of mixed overlapping elements in incompressible analysis. *Computer Methods in Applied Mechanics and Engineering*, 412:116104. https://doi.org/10.1016/j.cma.2023.116104

Zhang HW, Zhou L, 2006. Numerical manifold method for dynamic nonlinear analysis of saturated porous media. *International Journal for Numerical and Analytical Methods in Geomechanics*, 30(9):927-951. https://doi.org/10.1002/nag.508

Zhao Y, Choo J, 2020. Stabilized material point methods for coupled large deformation and fluid flow in porous materials. *Computer Methods in Applied Mechanics and Engineering*, 362:112742. https://doi.org/10.1016/j.cma.2019.112742

Zienkiewicz OC, Chang CT, Bettes P, 1980. Drained, undrained, consolidating and dynamic behaviour assumptions in soils. *Geotechnique*, 30(4):385-395. https://doi.org/10.1680/geot.1980.30.4.385

Zienkiewicz OC, Huang M, Wu J, et al., 1993. A New Algorithm for the Coupled Soil–Pore Fluid Problem. *Shock and Vibration*, 1(1):801536. https://doi.org/10.3233/SAV-1993-1102

Electronic supplementary materials

Sections S1–S3

中文概要

题　目：低渗透性饱和多孔介质动力分析有限元格式对比评估

作　者：潘安浩[1,2]，凌道盛[1,2]，缪骁[1,2]，郑建靖[2,3]

机　构：[1]浙江大学，岩土工程研究所，中国杭州，310058；[2]浙江大学，软弱土与环境土工教育部重点实验室，中国杭州，310058；[3]浙江大学，超重力研究中心，中国杭州，310058

目　的：针对低渗透饱和多孔介质动力响应等阶有限元分析中出现的虚假孔隙压力振荡问题，本文旨在比较两种主要的有限元公式：一种基于覆盖函数富集的新型不等阶插值单元，另一种为稳定化的等阶插值单元，以提高动力分析的精度和稳定性。

创新点：1. 基于覆盖函数富集的非等阶插值单元格式，分别构建了适用于一维问题的四边形单元和适用于二维问题的三角形单元，以解决覆盖单元中固有的线性相关问题；2. 系统对比了覆盖单元与稳定化等阶单元在可压缩与不可压缩材料条件下的数值性能，明确了稳定化方法在不同材料属性条件下的局限性及适用范围。

方　法：1. 构造了覆盖函数富集的不等阶插值单元和稳定化等阶插值单元；2. 通过典型数值算例，系统评估了两种单元在可压缩与不可压缩材料条件下的性能表现。

结　论：1. 覆盖单元在可压缩与不可压缩两种材料工况下均能一致且准确地捕捉孔隙压力的演化过程；2. 稳定化等阶单元仅在骨架刚度较高的不可压缩材料中可获得较高的计算精度，而在可压缩材料中性能显著下降。

关键词：覆盖函数；线性相关；不等阶单元；稳定化单元；孔压振荡